ELSEVIER

Comput. Methods Appl. Mech. Engrg. 151 (1998) 27–42

Computer methods in applied mechanics and engineering

On some recent adventures into improved finite element CFD methods for convective transport

A.J. Baker *, J.S. Iannelli, Subrata Roy [1], D.J. Chaffin

Mechanical and Aerospace Engineering and Engineering Science, University of Tennessee, Knoxville, TN 37996-2030

Abstract

The quest continues for computational fluid dynamics (CFD) algorithms that are accurate and efficient for convection-dominated applications including shocks, travelling fronts and wall-layers. The boundary-value 'optimal' Galerkin weak statement invariably requires manipulation, either in the test space or in an augmented form for the conservation law system, to handle the disruptive character introduced by the discretized first-order convection term. An incredible variety of methodologies have been derived and examined to address this issue, in particular seeking achievement of accurate and monotone discrete approximate solutions in an efficient implementation.

The UTK CFD research group continues its search on examining the breadth of approaches leading to development of a consistent, encompassing theoretical statement exhibiting quality performance. Included herein are adventures into generalized Taylor series (Lax–Wendroff) methods, characteristic Euler flux resolutions, sub-grid embedded high-degree Lagrange bases with static condensation, and assembled-stencil Fourier analysis optimization for finite element weak statement implementations. For appropriate model problems, including steady convection–diffusion and pure unsteady convection, and benchmark Navier–Stokes definitions, recent advances have lead to candidate accurate monotone methods with linear basis efficiency. This contribution highlights the theoretical developments, and presents quantitative documentation of achievable high quality solutions.

1. Introduction

The Navier–Stokes conservation law system for the state variable $q = q(x_j, t)$ is of the form

$$\mathcal{L}(q) = \frac{\partial q}{\partial t} + \frac{\partial}{\partial x_j}(\mathrm{f}_j - \mathrm{f}_j^v) - s = 0, \quad \text{on } \Omega \times t \subset \Re^d \times \Re^+, \quad 1 \leqslant j \leqslant d \tag{1}$$

where $\mathrm{f}_j = f(u_j, q)$ and $\mathrm{f}_j^v = f(\epsilon \partial q / \partial x_j)$ are the kinetic and dissipative flux vectors respectively, the convection velocity is u_j, $\epsilon > 0$ is the diffusion coefficient that varies parametrically and s is a source. Appropriate initial and boundary conditions close system (1) for the well-posed statement.

Computational difficulties occur as $\epsilon \to 0$, leading to occurence of 'thin layer' solutions containing large gradients, e.g., boundary layer, shock. In CFD, this is the natural occurrence for Reynolds number becoming large. Thereby, even though the analytical solution to (1) remains smooth, monotone and bounded, the spatially discretized CFD solution process becomes dominated by an oscillatory error mode, leading to instablity in the presence of the inherent Navier–Stokes non-linearity in f_j.

*Corresponding author.

[1] Currently at Technical Center, Case Corporation, Burr Ridge, IL 60521-6975, USA. rsubratacasecorp.com

PII S0045-7825(97)00121-7

Thus, a persistent CFD algorithm research goal is to obtain an efficient, multi-dimensional 'arbitrary' grid algorithm that extracts an accurate, stable and monotone solution for (1) on a *practical mesh* for arbitrary ϵ. Stabilizing techniques such as artificial viscosity methods [1–3] and/or flux correction operations [4, 5] contain one or more arbitrary parameters. Fluxvector splitting methods [6] replace parameters with switches, but solutions may still exhibit oscillations near strictly local extrema. Implementation of non-linear correction factors called *limiters* [7] requires a relatively dense mesh for interpolation to attain an essentially non-oscillatory (ENO) solution. Finally, most of these theories are developed via analysis on 1-D schemes, hence become theoretically tenuous in a multi-dimensional application.

'Intelligent' algorithms for handling solution mesh adaptation in an *automatic* manner have been extensively examined in finite element (FE) solution-adaptive '*p* and *h-p*' forms, [8–14]. Several advantages, including 'unstructured meshing,' accrue to these algorithms, but at a significant cost in increased algorithm operation count and storage requirements that can hinder achieving *practical mesh* solutions. Recent developments in the area of subgrid scale resolution include hierarchical (*h-p*) elements [15] and inclusion of nodeless bubble functions [16]. Solution monotonicity is typically not an ingredient in these theories, and as the number of degrees of freedom (DOF) increases, especially for 3-D, the algebraic system matrix order increases rapidly, hence also the computer resource requirement. Numerical linear algebra efficiency issues then also become a central issue.

This paper summarizes and develops the weak statement theory for some recent developments and documents performance for verification and benchmark problem statements belonging to the Navier–Stokes problem class, for smooth and non-smooth solutions including nonlinearity.

2. The weak statement formulation

The weak statement underlines the development of the range of CFD algorithms. Such an integral statement associated with (1) is

$$\int_{\Omega} w \left[\frac{\partial q}{\partial t} + \frac{\partial}{\partial x_j} \left(\mathrm{f}_j - \mathrm{f}_j^v \right) - s \right] \mathrm{d}\Omega = 0 \tag{2}$$

where w denotes any admissible test function. Thereafter, the finite element (FE) spatial semi-discretization of the domain Ω of (1) employs the mesh $\Omega^h = \bigcup_e \Omega_e$, and Ω_e is the generic computational domain. Using superscript 'h' to denote 'spatial discretization,' the FE weak statement implementation for (1)–(2) defines the approximation as

$$q(\boldsymbol{x}, t) \approx q^h(\boldsymbol{x}, t) = \bigcup_e q_e(\boldsymbol{x}, t) \tag{3}$$

$$q_e(\boldsymbol{x}, t) = \{N_k(\boldsymbol{x})\}^{\mathrm{T}} \{Q(t)\}_e \tag{4}$$

where $\{\cdot\}$ denotes a column matrix, and the trial space FE basis set $\{N_k(\boldsymbol{x})\}$ typically contains Chebyshev, Lagrange or Hermite interpolation polynomials complete to degree k, plus perhaps 'bubble functions' [16].

The spatially semi-discrete FE implementation of the *weak statement* WS^h for (1)–(2) leads to

$$\mathrm{WS}^h = S_e \left(\int_{\Omega^h} \{N_k\} \left(\frac{\partial q^h}{\partial t} + \frac{\partial}{\partial x_j} (\mathrm{f}_j - \mathrm{f}_j^v)^h - s \right) \mathrm{d}\tau \right) \equiv \{0\} \tag{5}$$

$$= S_e \left(\int_{\Omega^h} \{N_k\} \left(\frac{\partial q^h}{\partial t} - s \right) \mathrm{d}\tau - \int_{\Omega^h} \frac{\partial \{N_k\}}{\partial x_j} (\mathrm{f}_j - \mathrm{f}_j^v)^h \, \mathrm{d}\tau + \oint_{\partial\Omega_e \cap \partial\Omega^h} \{N_k\} (\mathrm{f}_j - \mathrm{f}_j^v)^h \, \hat{n}_j \, \mathrm{d}\sigma \right) \tag{6}$$

using the Green–Gauss divergence theorem and S_e symbolizes the 'assembly operator' carrying local (element) matrix coefficients into the global arrays. The surface integral in (5) contains the unknown boundary fluxes wherever Dirichlet (fixed) boundary conditions are enforced.

Independent of the dimension d of Ω, and for general forms of the flux vectors, the FE semi-discretized weak statement (5) always yields an ordinary differential equation (ODE) system

$$\mathrm{WS}^h = [M]\{Q(t)\}' + \{R\} = \{0\} \tag{7}$$

where $\{Q(t)\}'$ denotes $\mathrm{d}\{Q\}/\mathrm{d}t$, and the system square matrix $[M]$ and 'residual' column matrix $\{R\}$ are formed via assembly over $\Omega^h = \bigcup \Omega_e$ of corresponding element rank matrices as

$$[M] = S_e[M_k]_e \quad \text{and} \quad \{R\} = S_e\{R_k\}_e = S_e(([U]_e + [D]_e + [B]_e)\{Q\}_e - \{b\}_e) \tag{8}$$

where subscript k in (8) emphasizes coefficient dependence on FE basis degree k in (4). On each finite element Ω_e, the contained compositions are $[D]_e$ for the dissipative fluxvector f_j^v, $[U]_e$ for the convective flux vector f_j, and $[B]_e$ for the $d-1$ dimensional implimentation of the boundary flux contribution, while $\{b\}$ is the matrix of all known data.

The form (7) provides the local time derivative necessary to evaluate a temporal Taylor series (TS). Selecting the θ-implicit one-step Euler family, then

$$\{Q(t_{n+1})\} \equiv \{Q\}_{n+1} = \{Q\}_n + \Delta t\,[\theta\{Q\}'_{n+1} + (1-\theta)\{Q\}'_n] + \mathcal{O}\left(\Delta t^{f(\theta)}\right) \tag{9}$$

$$= \{Q\}_n - \Delta t\,[M]^{-1}(\theta\{R\}_{n+1} + (1-\theta)\{R\}_n) + \mathrm{H.O.T.}$$

where subscript n denotes time level. Clearing $[M]^{-1}$ and collecting terms to a homogeneous form yields the $\mathrm{WS}^h + \theta\mathrm{TS}$ terminal algorithm statement

$$\{FQ\} = [M]\{Q_{n+1} - Q_n\} + \Delta t(\theta\{R\}_{n+1} + (1-\theta)\{R\}_n) = \{0\} \tag{10}$$

The *Newton algorithm* for solution of (10) is

$$[\mathrm{JAC}]\{\Delta Q\}_{n+1} = -\Delta t\{R\}_n, \quad \text{linear} \tag{11}$$

$$[\mathrm{JAC}]\{\delta Q\}^{p+1} = -\{FQ\}^p_{n+1}, \quad \text{non-linear} \tag{12}$$

where for iteration index p

$$\{Q\}^{p+1}_{n+1} \equiv \{Q\}^p_{n+1} + \{\delta Q\}^{p+1} = \{Q\}_n + \sum_{i=1}^{p} \{\delta Q\}^{i+1} \tag{13}$$

The linear form (11) converges in a single step, hence $\{Q\}_{n+1} = \{Q\}_n + \{\Delta Q\}_{n+1}$. In either instance, the Newton *jacobian* is formed as

$$[\mathrm{JAC}] = \frac{\partial\{FQ\}}{\partial\{Q\}} = [M] + \theta\Delta t\left(\frac{\partial\{R\}}{\partial\{Q\}}\right) \tag{14}$$

For the steady state problem, $\partial q/\partial t = 0$ in (1), hence clearing through the Δt in (10)–(14) yields $[\mathrm{JAC}] = \partial\{R\}/\partial\{Q\}$ and $\{FQ\} = \{R\}$.

3. The Taylor weak statement

Baker and Kim [1] generalized the methods of Lax and Wendroff [23] and Donea [24] as the 'Taylor Weak Statement.' The method is readily illustrated for multidimensional linear advection

$$\mathcal{L}(q) = \frac{\partial q}{\partial t} + u_j\frac{\partial q}{\partial x_j} = 0 \tag{15}$$

Higher derivatives are taken in the manner of Lax and Wendroff

$$\begin{aligned} \frac{\partial^2 q}{\partial t^2} &= -u_j\frac{\partial}{\partial x_j}\frac{\partial q}{\partial t} = u_k\frac{\partial}{\partial x_k}\left(u_j\frac{\partial q}{\partial x_j}\right) \\ \frac{\partial^3 q}{\partial t^3} &= u_k\frac{\partial}{\partial x_k}\left(u_j\frac{\partial}{\partial x_j}\frac{\partial q}{\partial t}\right) = -u_l\frac{\partial}{\partial x_l}\left(u_k\frac{\partial}{\partial x_k}\left(u_j\frac{\partial q}{\partial x_j}\right)\right) \end{aligned} \tag{16}$$

Convex combinations of the time and space derivative terms are taken using arbitrary weights $\alpha, \beta, \gamma, \mu$

$$\begin{aligned} \frac{1}{2}\frac{\partial^2 q}{\partial t^2} &= \alpha\left(u_j \frac{\partial}{\partial x_j}\frac{\partial q}{\partial t}\right) + \beta\left(u_k \frac{\partial}{\partial x_k}\left(u_j \frac{\partial q}{\partial x_j}\right)\right), \\ \frac{1}{6}\frac{\partial^3 q}{\partial t^3} &= \gamma\left(u_k \frac{\partial}{\partial x_k}\left(u_j \frac{\partial}{\partial x_j}\frac{\partial q}{\partial t}\right)\right) + \mu\left[u_l \frac{\partial}{\partial x_l}\left(u_k \frac{\partial}{\partial x_k}\left(u_j \frac{\partial q}{\partial x_j}\right)\right)\right], \end{aligned} \tag{17}$$

which when substituted into an explicit Taylor time series

$$q^{n+1} = q^n + \Delta_t \frac{\partial q^n}{\partial t} + \frac{\Delta_t^2}{2}\frac{\partial^2 q^n}{\partial t^2} + \frac{\Delta_t^3}{6}\frac{\partial^3 t^n}{\partial t^3} + \frac{\Delta_t^4}{24}\frac{\partial^4 q^n}{\partial t^4} + \mathcal{O}(\Delta_t^5) \tag{18}$$

and then substituted into (15) yields a 'Taylor-series corrected' semidiscrete form

$$\begin{aligned} \mathcal{L}(q) = \frac{\partial q}{\partial t} + u_j \frac{\partial q}{\partial x_j} \approx \frac{q^{n+1} - q^n}{\Delta_t} + u_j \frac{\partial q}{\partial x_j} - \Delta_t\left[\alpha\left(u_j \frac{\partial}{\partial x_j}\frac{q^{n+1} - q^n}{\Delta_t}\right) + \beta\left(u_k \frac{\partial}{\partial x_k}\left(u_j \frac{\partial q}{\partial x_j}\right)\right)\right] \\ - \Delta_t^2\left[\gamma\left(u_k \frac{\partial}{\partial x_k}\left(u_j \frac{\partial}{\partial x_j}\frac{q^{n+1} - q^n}{\Delta_t}\right)\right) + \mu\left[u_l \frac{\partial}{\partial x_l}\left(u_k \frac{\partial}{\partial x_k}\left(u_j \frac{\partial q}{\partial x_j}\right)\right)\right]\right] \end{aligned} \tag{19}$$

consisting of the 'standard' approximation plus correction terms $\alpha(\cdots)$, $\beta(\cdots)$, $\gamma(\cdots)$, and $\mu[\cdots]$. Each term in (19) can be approximated using linear basis finite elements except the last term $\mu[\cdots]$ which is normally set to zero for simplicity. The more useful of the correction terms are $\beta(\cdots)$, an artificial diffusion term, and $\gamma(\cdots)$, a time accuracy correction. Selecting these produces a 'Taylor weak statement' (TWS) generalized linear advection form which can replicate diverse schemes from the literature by using standard elements and assigning appropriate values to the constants. Values for schemes such as Petrov–Galerkin, Taylor–Galerkin, Characteristic–Galerkin, and QUICK are reported in [1, 22].

A standard Fourier or von Neumann analysis has been applied to the TWS statement to optimize transient or phase accuracy [22]. With fixed values of constants β and γ, the TWS form can replicate the unique fourth-order accurate (in frequency) one-dimensional finite difference scheme derived by several authors, probably first by Stone and Brian [25]. Although accuracy can be extended indefinitely using higer-order elements or wider stencils, this scheme uses a linear basis with three-wide node stencil for efficiency. The transient accuracy can be improved to fifth-order accurate by varying the constants with time, without increasing the stencil width. The phase accuracy can be further improved by optimizing the constants to minimize error rather than meeting a specific order of accuracy, these criteria being identical in the limit but different at (achievable) low orders of accuracy.

This frequency optimization is useful for pure transient problems as illustrated by the 'cosine hill' or 'rotating cone'. Its initial condition and analytical solution after one revolution are shown in Fig. 1 and the uncorrected trapezoidal rule finite element solution after one revolution in Fig. 2. This simulation was run with Courant number of 1/2 and shows substantial dispersion error waves.

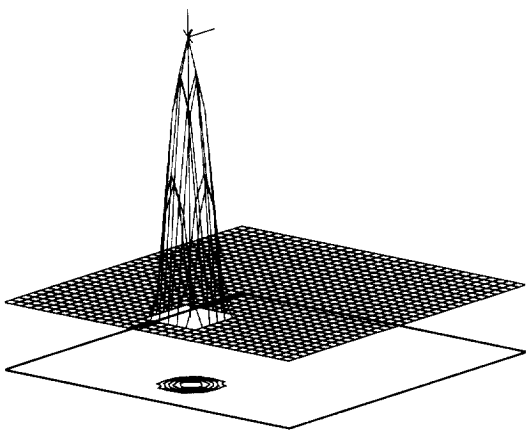

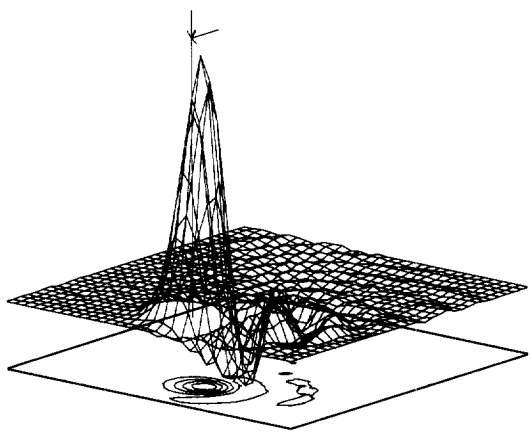

Fig. 1. Analytical rotating cone.

Fig. 2. Standard trapezoidal rule.

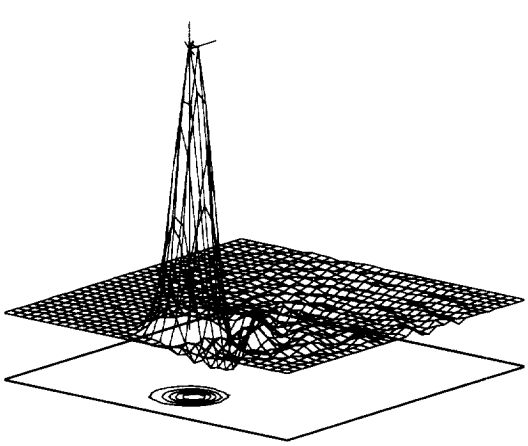

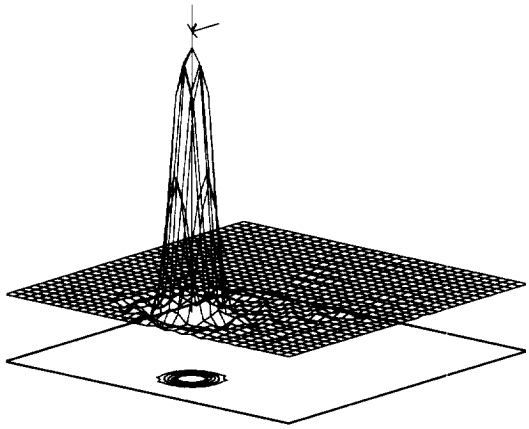

Fig. 3. Fourth-order corrected.
Fig. 4. Phase-optimized.

The fourth-order corrected TWS solution is shown in Fig. 3, while the phase-optimized TWS solution is given in Fig. 4. Each solution shows improvement over the Galerkin form, Fig. 2, in regards to accuracy and phase error reduction.

Work continues on optimizing the TWS methodology for stability using artificial diffusion and using TWS on nonlinear equation systems.

4. NEWS: Non-linear element upstream weak statement

NEWS is a Galerkin finite element discretization of the Navier–Stokes 'characteristics' integral weak statement

$$\int_{\Omega} w \left[\frac{\partial q}{\partial t} + \frac{\partial}{\partial x_j}(\mathrm{f}_j^C - \mathrm{f}_j^v) - s \right] \mathrm{d}\Omega = 0 \tag{20}$$

associated with (2) where f_j^C denotes the characteristics resolution of the Euler flux f_j. The flux f_j^C in the discrete weak statement (5) yields a multidimensional characteristics consistent formulation that induces minimal dissipation. This flux, in fact, will automatically yield an upstream-bias discretization of $\partial \mathrm{f}_j / \partial x_j$, along characteristic directions, but only in regions of solution discontinuities. In regions of solution smoothness, f_j^C will approach f_j. In this manner, the induced dissipation remains focused in regions of solution discontinuities, without adversely affecting the smooth parts of the solution.

Following a characteristics decomposition of the multi-dimensional flow field into multi-dimensional acoustics, convection, and pressure-gradient fields [26], the corresponding resolution of the Euler flux for accurate approximation of flow wave propagation is expressed for a representative 2-D formulation as

$$\mathrm{f}_j^C \equiv \mathrm{f}_j - \varepsilon\psi \left[c\,(\beta\, a_j\, a_\ell + \beta^N a_j^N a_\ell^N)\, \frac{\partial q}{\partial x_\ell} + a_j \left(\frac{\partial \mathrm{f}_\ell^q}{\partial x_\ell} + \delta \frac{\partial \mathrm{f}_\ell^p}{\partial x_\ell} \right) \right] \tag{21}$$

where the expression between brackets corresponds to the contraction of an upstream-bias tensor with the gradient of q and generalizes the traditional 'numerical-flux' formulae.

In this tensor contraction, the first two terms denote the acoustics component, which for high subsonic and for supersonic Mach numbers remains by design non-negligible only within a narrow multi-

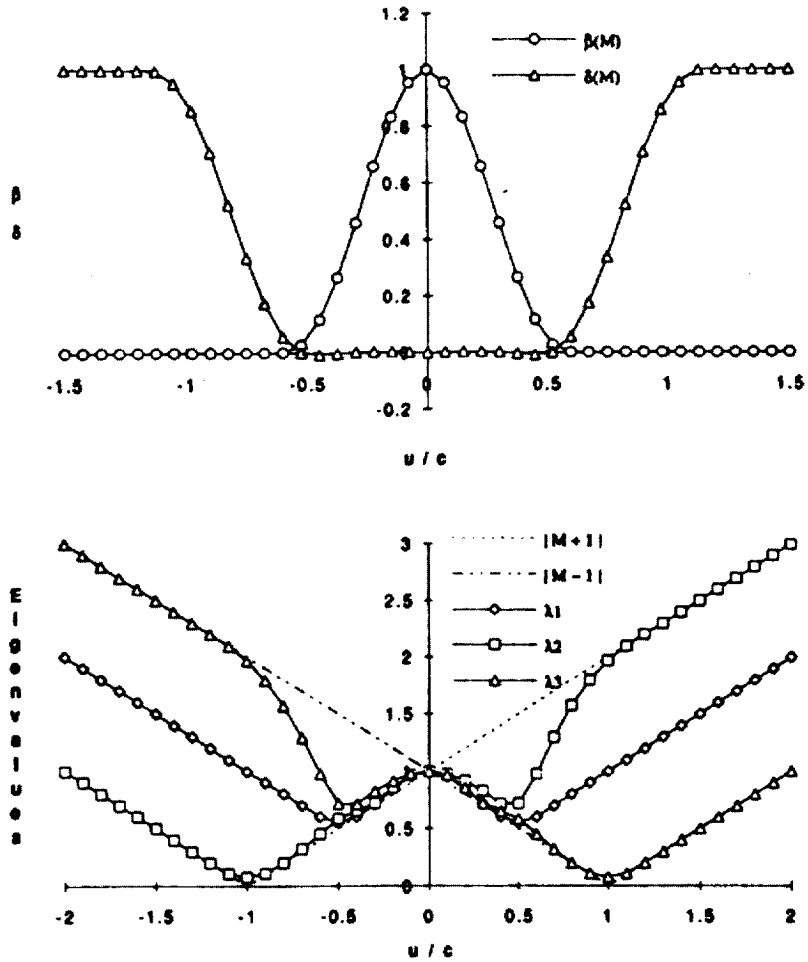

Fig. 5. (a) Upstream-bias functions β and δ vrsus u/c; (b) Upstream-bias stream wise eigenvalues versus u/c.

dimensional conical region about the cross flow direction. As its name indicates, the acoustics component originates as an exact Riemann solver for the acoustics limit of the full Euler equations. The two terms between parentheses denote the convection and pressure-gradient components, which originate from a decomposition of the divergence of the Euler inviscid flux vector f_j. In these two terms, $\partial(\mathrm{f}_j^p)/\partial x_j$ corresponds to the pressure gradient in the momentum equations and $\mathrm{f}_j^q \equiv \mathrm{f}_j - \mathrm{f}_j^p$.

In the tensor contraction in (21), the positive variables ε and ψ indicate a reference length and the upstream-bias 'smoothess' controller. In regions of solution discontinuities, $\psi = 1$, so that (21) induces a finite amount of upstream-bias; in regions of solution smoothness, ψ substantially decreases so that f^C approaches f_j. The variables $\boldsymbol{a}=\boldsymbol{a}(q)$ and $\boldsymbol{a}^N=\boldsymbol{a}^N(q)$ in (21) correspond to unit vectors parallel and perpendicular to the flow velocity. Additionally, $c = c(q)$ denotes the local speed of sound, $\beta = \beta(M)$ and $\beta^N = \beta^N(M)$ are two Mach-number-dependent upstream-bias functions so that $\beta(0) = \beta^N(0) = 1$, i.e. the acoustics limit, and $\beta(M) \equiv 0$ for $M \geqslant M_s$, where M_s denotes a subsonic threshold Mach number; the function $\beta^N(M)$, instead, remains positive and approaches zero as M increases. The function $\delta = \delta(M)$ indicates a scalar pressure-gradient influence function, with $0 \leqslant \delta(M) \leqslant 1$, $\delta(0) = 0$ and $\delta(M) = 1$ for $M > 1$.

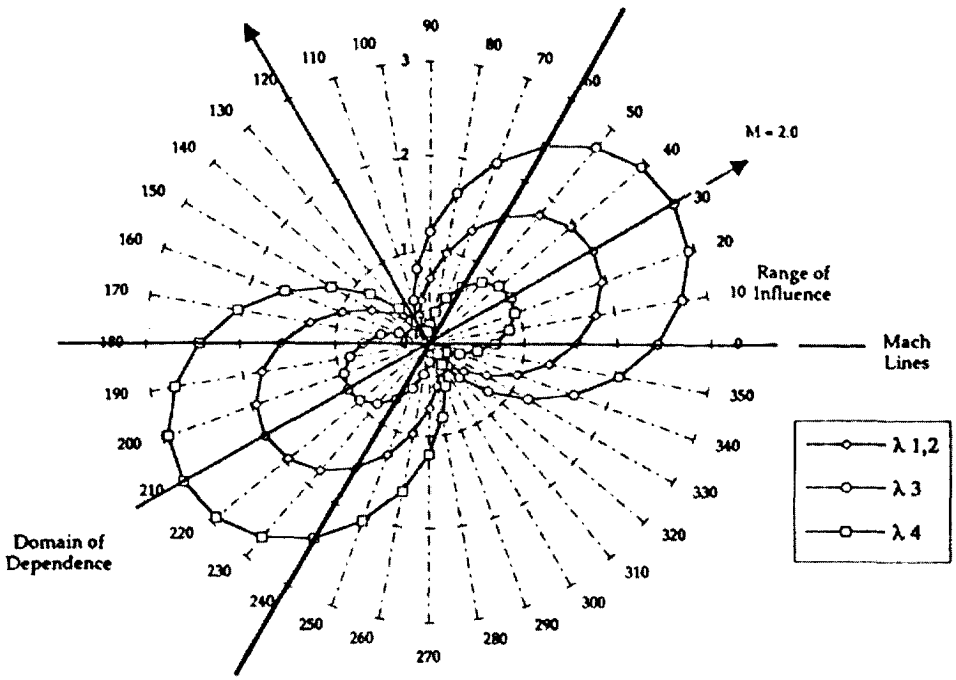

Fig. 6. Polar variation of upstream-bias eigenvalues, $M_\infty = 2.0$.

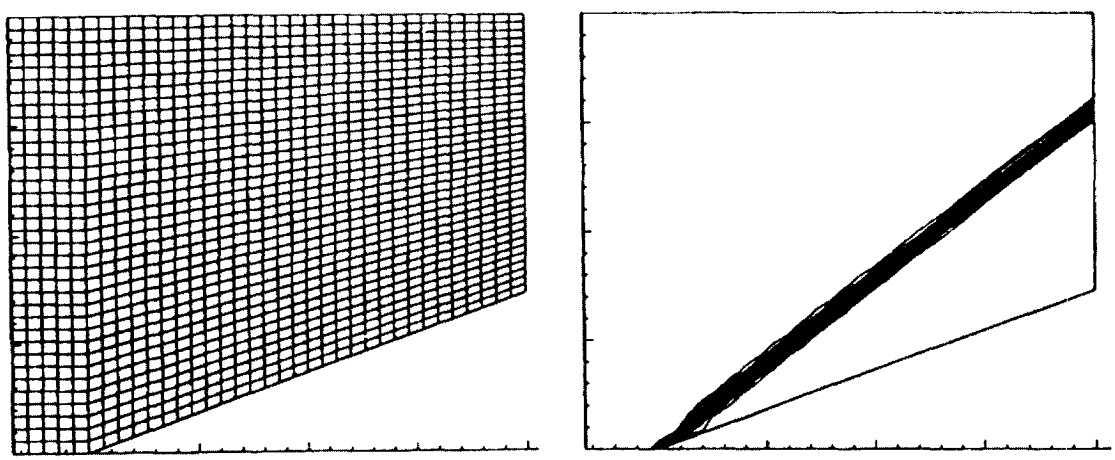

Fig. 7. $M_\infty = 3.0$ Compression ramp, (a) NEWS 35 × 35 element grid; (b) NEWS density contours.

Within a multi-dimensional flow-field, flow waves propagate in infinitely many directions. The upstream-bias tensor will therefore allow an accurate approximate propagation of waves when it induces an upstream-bias in all flow directions. This tensor, therefore, must remain consistent and globally stable; its eigenvalues, therefore, must remain real and non-negative along all propagation directions radiating from any point within the flow field. Specific expressions for the upstream-bias functions $\beta(M)$, $\beta^N(M)$ and $\delta(M)$ were thus determined by enforcing this demanding global stability condition on the upstream-bias tensor. These functions remain differentiable as shown in Fig. 5a.

Despite the formidable structure of the non-linear upstream-bias tensor in (21), its characteristic eigenvalues have all been exactly determined in analytical closed form for arbitrary 3-D flow states [26], and it was found that the principal axes of this tensor are in the streamwise and cross flow directions. Correspondingly, the characteristic eigenvalues attain their maximum values in the streamwise direction, a characteristic direction for the steady multi-dimensional Euler equations. These streamwise eigenvalues remain continuous and differentiable in the subsonic, transonic, and supersonic Mach number regime, and smoothly merge into the classical M, $M+1$ and $M-1$ eigenvalues in the supersonic regime, beginning at the critical $M=1$ neighborhood, as presented in Fig. 5b.

The analysis of the directional variation of the characteristic eigenvalues for all flow directions and Mach numbers indicates that the upstream-bias tensor induces anisotropic variable-strength upwinding in which the magnitude of the streamwise and cross flow dissipations remain different from and independent of each other. The streamwise dissipation depends on the Mach number and the cross flow dissipation decreases for increasing Mach number and becomes negligible for supersonic flows, as indicated in Fig. 6, which presents the polar variation of the upstream-bias eigenvalues about a velocity vector at 30° with respect to the horizontal x-axis. In this manner, therefore, the developed formulation will not generate for increasing M as much cross wind dissipation as induced by an isotropic or direction-split perturbations. As a further result of this analysis, not only is the acoustics perturbation important for accurate approximate acoustic wave propagation, but it is also pivotal for global stability. In fact, without acoustics perturbation, the characteristic eigenvalues turn negative, hence unstable, within a conical region about the cross wind direction [26]. Fig. 7b documents performance of the formulation for a compression-ramp $\mathrm{Ma}_\infty = 3.0$ supersonic flow. The captured density oblique shock remains essentially non-oscillatory and freely crosses the outflow boundary without any spurious reflection.

5. Sub-grid embedded (SGM) element

In distinction to [1–16], the sub-grid embedded (SGM) finite element basis theoretical development [27] addresses the fundamental issue of multi-dimensional *practical (coarse) grid solution accuracy with guaranteed monotonicity* and minimal (optimal) numerical diffusion. It is based on a genuinely non-linear, non-hierarchical, high-degree finite element basis for use in a discretized approximation of a weak statement algorithm. Verification for both linear and non-linear convection–diffusion equation SGM finite element solutions is documented in [27], cf. Fig. 8, where small ϵ ($\mathcal{O}10^{-5}$) monotone and nodally accurate solutions are obtained on coarse grids.

The SGM basis construction is distinct from reported developments in the area of subgrid scale resolution, including hierarchical (h-p) elements [15] and nodeless bubble functions [16]. The SGM development employs strictly classical Lagrange basis methodology, and the SGM basis is applicable *only* to the dissipative flux vector term f_j^v in (1), [28]. The discretized kinematic flux vector f_j remains a 'centered' construction via the parent strictly Galerkin weak statement.

The key efficiency ingredient of the SGM element is reduction to linear basis element matrix rank for any embedded degree. This is in sharp contrast to conventional enriched basis FE/FD algorithms, as the SGM element strictly contains matrix order escalation, hence increased computer resource demands.

The SGM theory augments the diffusion term in (5) via an *embedding* function $g(x,c)$, hence the name 'SubGrid eMbedded.' The definite integral form of the SGM basis function set, denoted $\{N_S\}$, for $[D]_e$ in (8) is

$$\int_{\Omega_e} \frac{\partial\{N_S\}}{\partial x}\frac{\partial\{N_S\}^{\mathrm{T}}}{\partial x}\,\mathrm{d}x = \int_{\Omega_e} g(x,c)\frac{\partial\{N_k\}}{\partial x}\frac{\partial\{N_k\}^{\mathrm{T}}}{\partial x}\,\mathrm{d}x\Bigg|^R \tag{22}$$

where the statically condensed, [19, 20], reduced Rank form is denoted as $|^R$. The embedded polynomial $g(x,c)$ contains one arbitrary (at present) parameter c for each additional Lagrange degree $k \geqslant 2$. The form of the 1-D SGM element basis set $\{N_S\}$ for $k = 2 = S$ is expressed, analogous to the $k = 1$ Lagrange basis, as

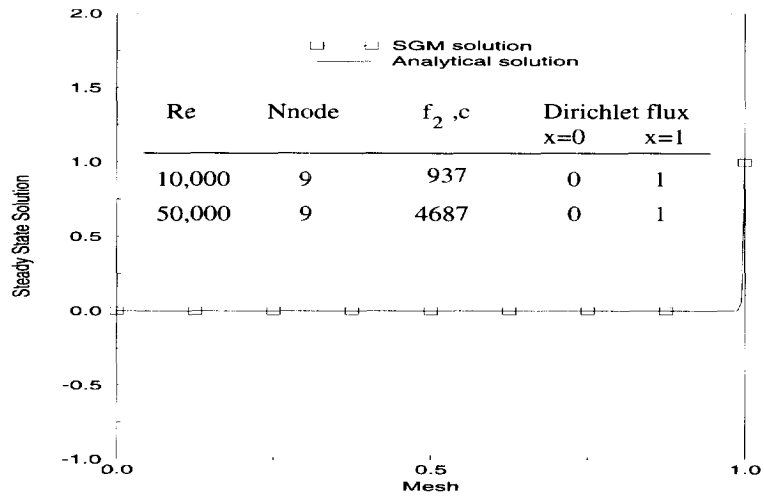

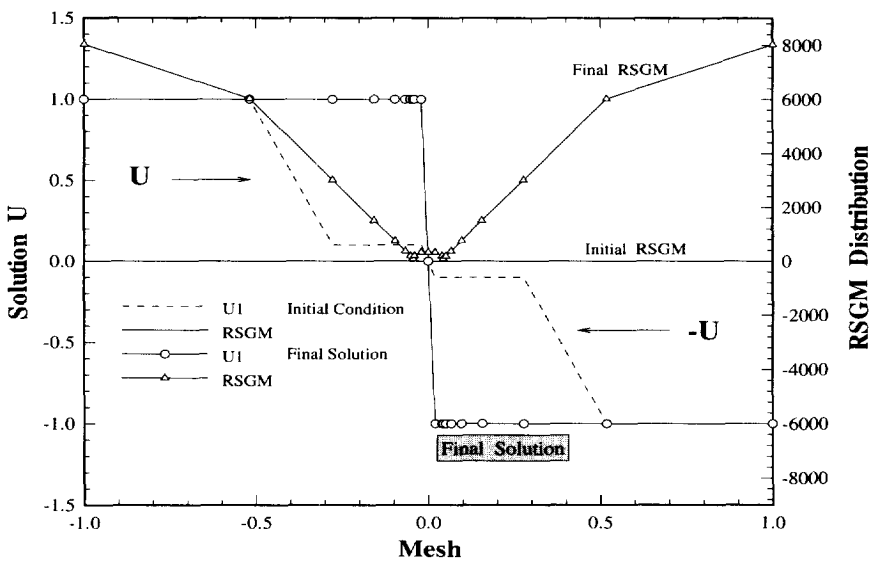

Fig. 8. Steady state SGM element solutions for convection–diffusion verification problems. (a) Linear Peclet problem, $1/\epsilon = \mathrm{Pe} \leqslant 5 \times 10^4$; (b) Non-linear Burgers initial and final solution at $1/\epsilon = \mathrm{Re} = 10^5$.

$$\{N_S\} = \begin{Bmatrix} 1-\mu \\ \mu \end{Bmatrix}, \quad \text{but } \mu = \sum_{i=1}^{\infty} a_i \zeta_i^{\alpha} \tag{23}$$

In (23), μ is a polynomial function of an expansion coefficient set, a_i, dependent on embedding degree k, and the $k = 1$ element local coordinate ζ, and α is a function of c.

The Lagrange linear ($k = 1$) and quadratic ($k = 2$) FE basis polynomial set, the $k = 1, p = 2$ hierachical (bubble) element, and the SGM $S = 2$ ($k = 2$, reduced) Lagrange element for 1-D and 2-D are compared in Fig. 9a-f. Both the Lagrange $k = 2$ and p-hierarchical elements contain an extra degree of freedom (node **2** in Fig. 9(b) and (c)). For the choice of quadratic embedded polynomial $g_2 = \{1, c, 1\}\{N_2\}$ in (22), where $\{N_2\}$ is the Lagrange quadratic basis, the SGM element is supported on only two nodes, Fig. 9(d). The discussion in [27] confirms $c \geqslant 1$ is the requirement. For $c \equiv 1$, the 1-D diffusion matrix is identical to the linear Lagrange 1-D diffusion matrix.

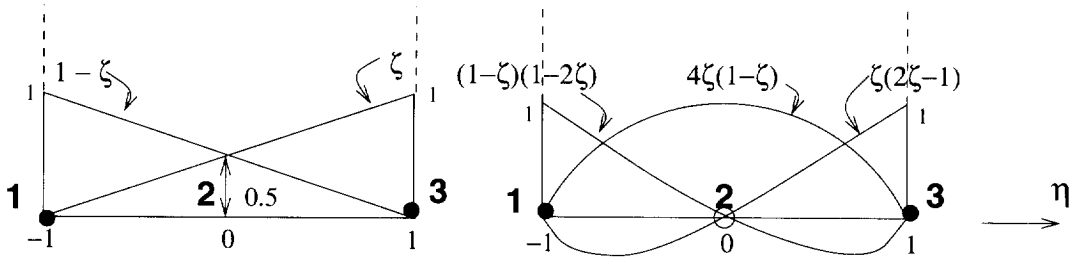

a) 1-D Lagrange element, k=1

b) 1-D Lagrange element, k=2

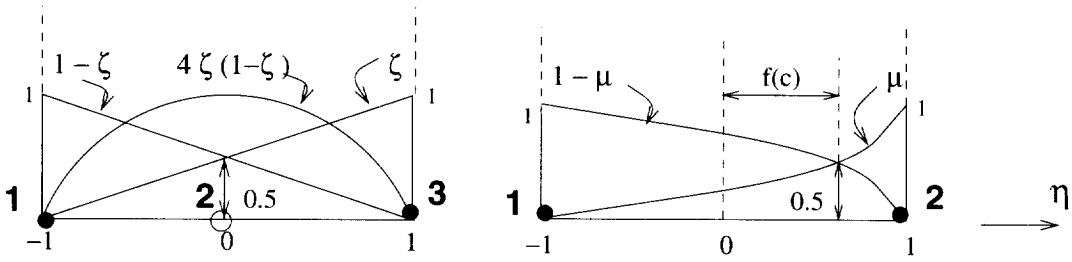

c) 1-D hierarchical element, k=1, p=2

d) 1-D SGM Lagrange element, k=2 reduced

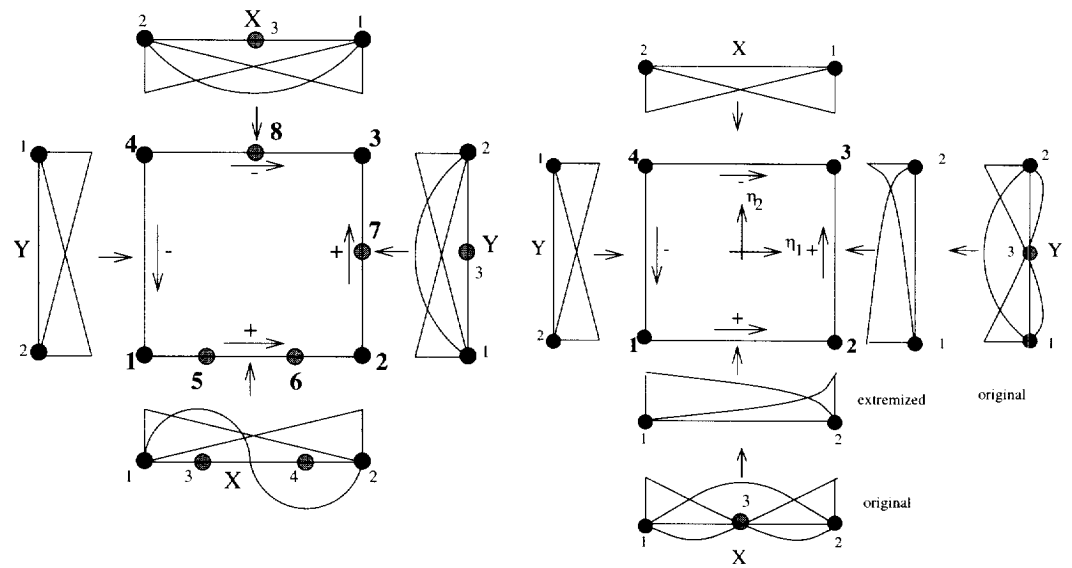

e) 2-D hierarchical p-element, k=1,2,3 selectively

f) 2-D SGM element, S=2

Fig. 9. Comparison of standard, hierarchical and SGM elements.

The SGM element construction for a 1-D model form of (1) leads to a theoretical *non-linear* monotonicity constraint via enforcement of a real eigenvalue spectrum for the algorithm stencil. Thereby, the theory predicts the optimal distribution of the SGM embedded parameter (set) on each element, hence the mesh Ω^h. The generalization to non-uniform, d-dimensional discretizations leads to the potential for attainment of nodally exact monotone solutions on arbitrary meshes. The multidimensional form of the nodally distributed SGM solution monotonicity constraint is directional and the parameter is derived as a function of convection velocity, mesh projection and Reynolds number [27].

5.1. Quasi-1D compressible de Laval nozzle shock verification

A quasi-one dimensional compressible Navier–Stokes problem SGM solution is documented. The normalized variable crossection is defined for a de Laval nozzle geometry, Fig. 10a, using the problem specification of [29]. The non-dimensional initial condition for state variable q is the sonic throat, shock-free isentropic solution. The reference state is inflow. The corresponding inlet Mach number is $\mathrm{Ma}_{\mathrm{in}} = 0.2395$.

The verification problem definition is the steady state following an impulsive change from isentropic flow by decreasing the exit pressure. The resultant expansion wave propagates upstream to the throat, hence triggers formation of a (normal) shock which moves downstream. The analytical solution shock Mach number and location is given in [30].

The nozzle domain is uniformly discretized into 50 elements. The non-dissipative GWS algorithm solution diverges for this problem. The TWS dissipative algorithm for $\beta \Rightarrow \beta_q = 0.1 - 0.2$ converges to a steady state with shock location and sharpness, hence non-monotone character, as a function of β, Fig. 10(b). A close look near the shock region reveals that the TWS $\beta = 0.2$ solution is substantially diffused, while the $\beta = 0.1$ solution is non-monotone (oscillatory). The SGM solution Mach number distribution at $\mathrm{Re} = 10^6$ is also plotted in Fig. 10(b). It is monotone and follows the analytical solution more closely than either TWS solution. Figure 10(c) verifies the monotonicity of the SGM solution during time evolution to steady state. Finally, the SGM solution on a non-uniform mesh is monotone and accurately captures the steady state shock on two nodes, Fig. 10(d). The analytical solution is plotted thereon for comparison, documenting that this non-uniform mesh SGM solution as essentially the Lagrange interpolant of the exact solution. The iteratively-determined SGM parameter set is plotted in Fig. 10(e). For $\mathrm{Re} = 10^6$, the parameters range between $10^3 - 10^4$, and a sharp shock point operator is confirmed present.

5.2. Gaussian plume, directional diffusion in a 3-D convective field

The standard benchmark problem ([19, Ch. 4.12]) calls for prediction of the steady-state convective-diffusive transport of a neutrally-buoyant contaminant introduced into a directional uniform velocity field in three dimensions. The diffusion tensor is orthotropic with negligible component parallel to the onset flow direction. This problem was devised to verify CFD methods applied to atmospheric transport of a contaminant continuously emitted from a point source. Computationally, the 'point' is distributed over a block of eight cells in a pyramidal distribution.

The governing PDE with orthotropic diffusion tensor in principal coordinates is

$$\frac{\partial q}{\partial t} + u_j \frac{\partial q}{\partial x_j} - \frac{\partial}{\partial x_i}\left(\epsilon_{(i)}\delta_{ij}\frac{\partial q}{\partial x_j}\right) - s = 0, \quad \text{on } \Omega \times t \subset \Re^3 \times \Re^+ \tag{24}$$

For the standard benchmark, the uniform imposed velocity field is $\boldsymbol{u} = 1\,\boldsymbol{i} + 0\,\boldsymbol{j} + 0\,\boldsymbol{k}$ with $\epsilon_1 = 0$, $\epsilon_2 = 0.02 = \epsilon_3$. For these specifications, the Lagrange $k = 1$ and $k = 2$ WS algorithm solutions produce accurate plume prediction with modest select negative concentrations predicted about the source, [19]. To better quantify dispersion error annihilation via SGM, $\boldsymbol{u} = 1\,\boldsymbol{i} + 1\,\boldsymbol{j} + 1\,\boldsymbol{k}$ is preferred with significantly decreased diffusion levels. Hence, $\epsilon_1 = 0.0001$, $\epsilon_2 = 0.1$ and $\epsilon_3 = 0.001$ are defined for (24).

The uniform $17 \times 17 \times 21$ standard benchmark computational mesh is retained with domain span an 80 km cube. For the modified velocity field, the source was moved to lie on the domain diagonal near the lower left domain corner. The Lagrange $k = 1$ WS algorithm steady-state solution predicts ranges of negative concentration, Fig. 11(a), with extremum -6%. The comparison $S = 2$ SGM solution, Fig. 11(b), is absolutely monotone, hence totally devoid of any negative concentration. Elsewhere, the $k = 1$ and $S = 2$ solution fields are nominally nodally identical.

6. Galerkin matrix perturbation (GMP) algorithm

For a large class of computational fluid dynamics (CFD) problems, the discrete approximate solution error is viewed as a truncation of a Taylor series expansion. A weak statement Galerkin matrix pertur-

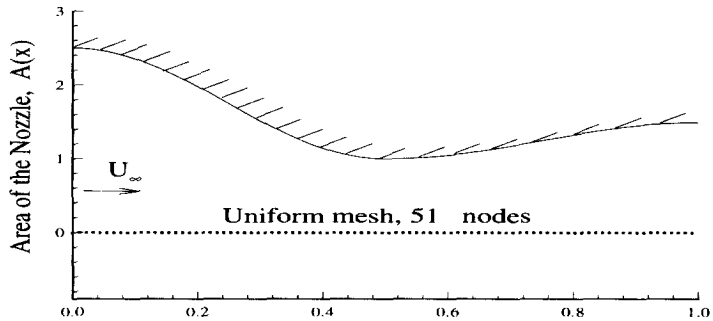

a) de Laval nozzle geometry

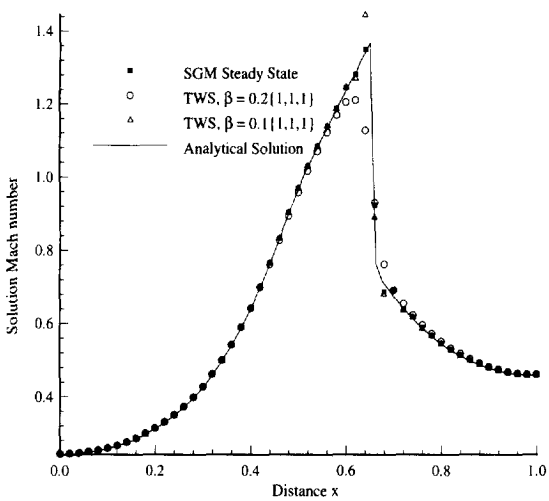

b) TWS and SGM comparison on uniform mesh

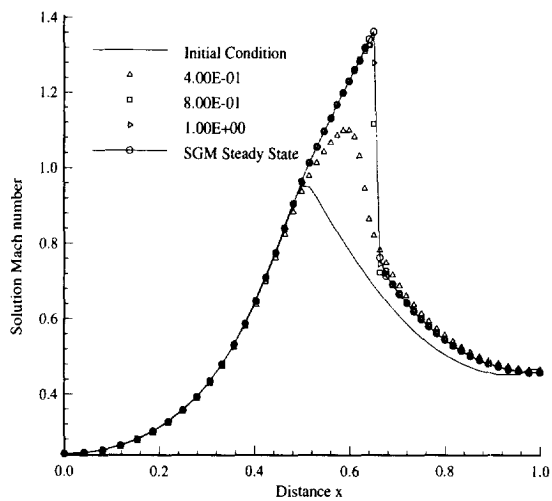

c) Time evolution of SGM solution

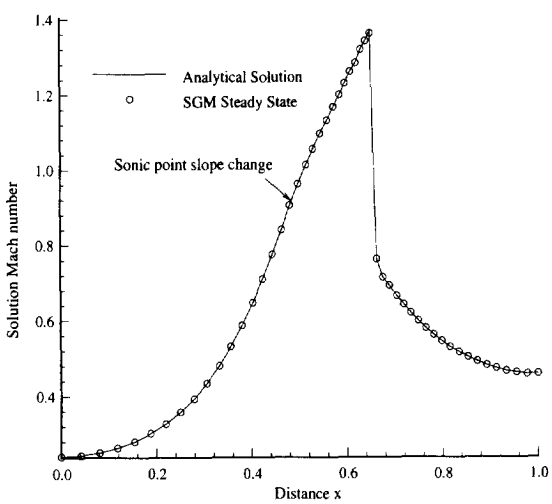

d) SGM solution on 51 node non-uniform mesh

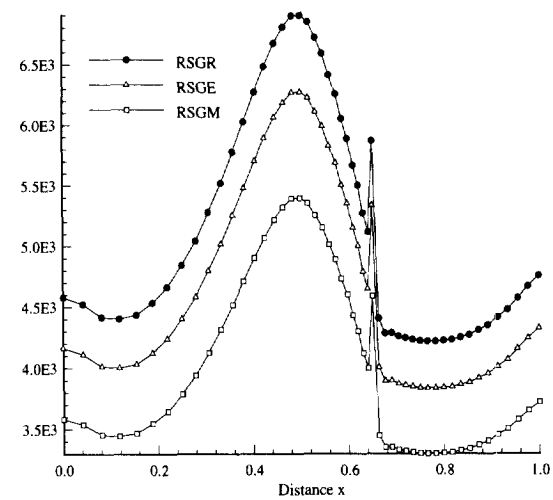

e) Steady state distributed SGM parameter $rsgm_q$

Fig. 10. Steady state solution Ma and $rsgm_q$ distribution for compressible flow, Re = 10^6.

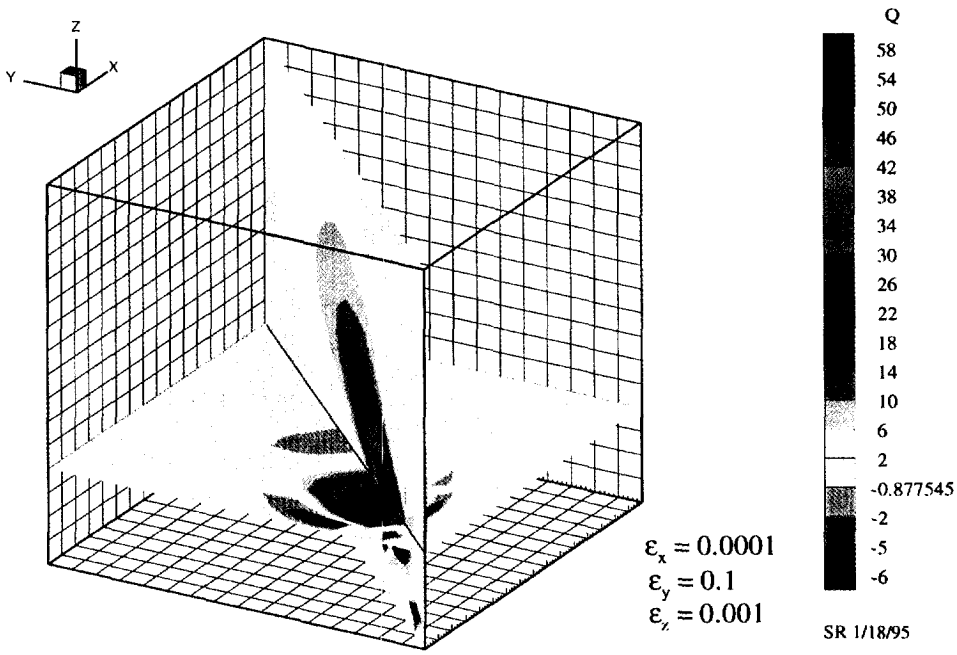

a) 3-D Plume Steady State GWS Solution

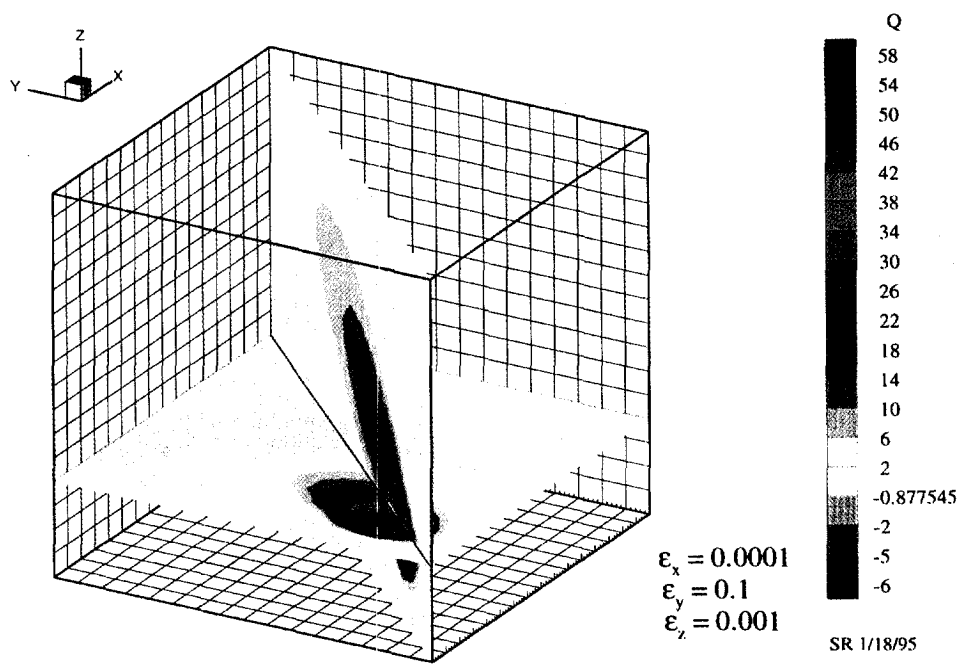

b) 3-D Plume Steady State SGM Solution

Fig. 11. 3-D Gaussian plume convection–diffusion solutions.

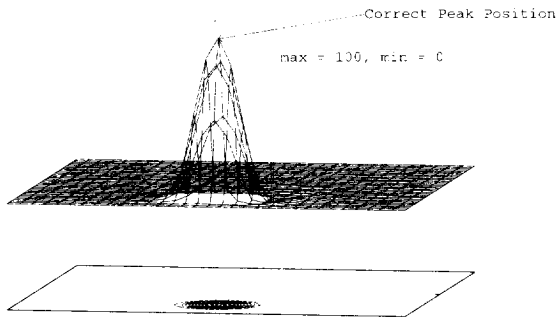

(a) initial condition and exact final solution

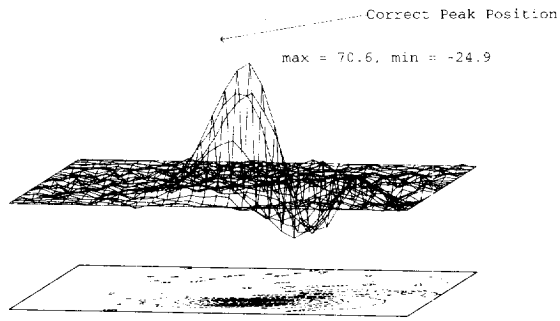

(b) $k = 1$ FE GWS, $C = 1$

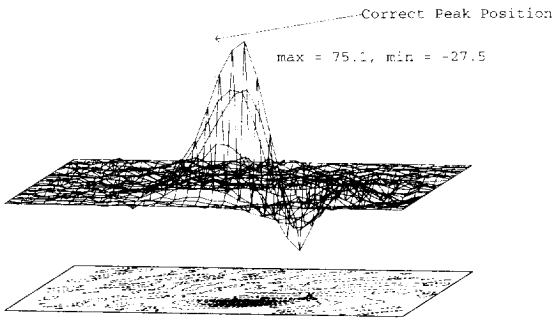

(c) $k = 2$ FE GWS, $C = 1$

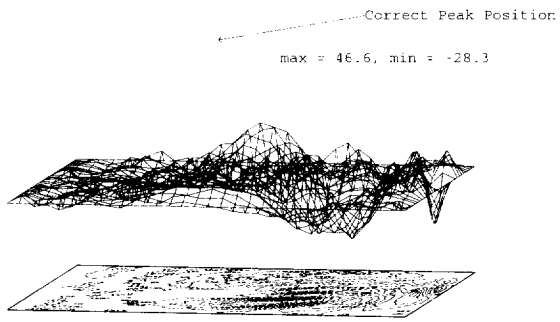

(d) Crank–Nicolson FD, $C = 1$

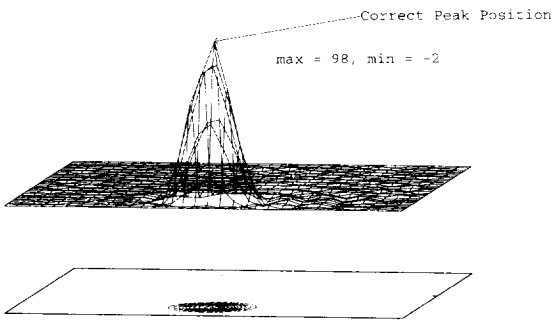

(e) h-p FE, $C \sim 1/6$, $\Delta t = 2\pi/400$

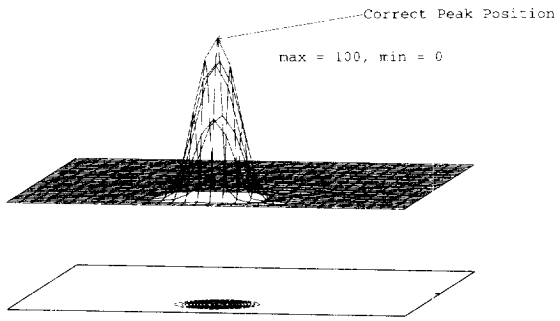

(f) GMP solution, $C_e = 1$, $\Delta t = 2\pi/32$

Fig. 12. Rotating cone solutions, one revolution on a 33×33 mesh.

bation (GMP) method is developed [31] yielding simple tridiagonal forms that reduce, or annihilate in special cases, the Taylor series truncation error. The procedure is analyzed via a von Neumann frequency analysis and can be theoretically compared with a wide class of algorithms, e.g. Taylor Weak Statement (TWS) and compact finite difference schemes on a term by term basis.

The algorithm amplification factor G determines how the fully discrete solution grows or decays in time. For the temporal and spatial discretization measure δt and δx, the 1-D analytical amplification factor for (15) may be expanded in a Laurent series as

$$G = \exp(-\mathrm{i}wu(n\,\delta t)) = \exp(-\mathrm{i}mC) = 1 - \mathrm{i}mC - (mC)^2/2! + \cdots \tag{25}$$

where $m = \omega\,\delta x$ is the virtual non-dimensional wavenumber with $C = u\,\delta t/\delta x$ the corresponding Courant number.

The discrete approximation solution amplification factor G^h is algorithm specific and may be computed via a Fourier modal analysis of the discretized CFD recursion relation. The order of accuracy, hence stability, of a numerical algorithm may be determined from its amplification factor G^h by matching coefficients of powers in wavenumber in the Laurent series expansion with the analytical solution G in (25).

Assuming that an arbitrary order of the Taylor series truncation error for the temporal and spatial discretization may be expressed in the form of FE perturbation matrices, the temporal and convection matrices of linear basis rank form become

$$[M] = S_e([M]_e - [APERT]_e) \tag{26}$$

$$\{R\} = S_e(([U]_e - [APERX]_e)\{Q(t)\}_e - b(t)) \tag{27}$$

where $[APERT]_e$ and $[APERX]_e$ are element level pertubation matrices that may be determined via comparing the Laurent series of the algorithm G^h and matching arbitrary coefficients for order accuracy with the Laurent series of G in (25), [31]. The forms of the elements of $[APERT]_e$ and $[APERX]_e$ are a sum series of $a_r\exp(\mathrm{i}mr), 0 \leqslant r \leqslant \gamma$, where a's are determinable coefficient and γ estimates the order of accuracy of the algorithm. Detailed descriptions for arbitrary order-accurate algorithms are available in [31]. For example, $\gamma = 0$ yields a general fourth-order accurate algorithm while $\gamma = 2$ is at least sixth-order accurate. However, as a special case, for $C = 1$ the $\gamma = 0$ perturbed mass matrix annihilates the phase dispersion error completely.

Verification hyperbolic solution is given for predicting the propagation of a cone initial distribution in a rotational convective field confirming theoretical prediction of high-order accuracy for GMP algorithm, Fig. 12(a–f).

7. Conclusions

Weak statement theory provides a rich basis for construction of CFD algorithms for the Navier–Stokes equations. The conception of the finite element basis function as the foundation for conversion to a computable form is fundamental to the implementation. This paper has presented a range of variations on the selection of traditional and non-traditional Lagrange basis forms designed for control and annihilation of the short wavelength dispersion error that dominates the computational process. In addition to providing a rational basis for selection/design, the procedures are capable of recovering a range of schemes derived by alternative means within a rational, hierarchical theory that provides guidance for the next level of developments.

References

[1] A.J. Baker and J.W. Kim, Int. J. Numer. Methods Fluids 7 (1987) 489–520.
[2] P.D. Lax, Comm. Pure Appl. Math. 7 (1954) 159–193.
[3] H.O. Kreiss and J. Lorenz, Initial-Boundary Value Problems and the Navier–Stokes Equations (Academic Press, New York, 1989).
[4] J.P. Boris and D.L. Book, J. Comput. Phys. 11 (1973) 38–69.
[5] S.T. Salezak, J. Comput. Phys. 31 (1979) 355–362.
[6] B. Van Leer, Proc. 8th Int. Conf. Numer. Methods Fluid Dyn. (Springer Verlag, 1982).
[7] H.T. Huynh, SIAM J. Numer. Anal. 30 (1993) 57–100.
[8] I. Babuška, B.Q. Guo and E.P. Stephan, Math. Methods Appl. Sci. 12 (1990) 413–427.

[9] L. Demkowicz, A. Karafiat and J.T. Oden, Comput. Methods Appl. Mech. Engrg. 101 (1992) 251–282.
[10] S. Jensen, Comput. Methods Appl. Mech. Engrg. 101 (1992) 27–41.
[11] C. Johnson and P. Hansbo, Comput. Methods Appl. Mech. Engrg. 101 (1992) 143–181.
[12] J.T. Oden, TICOM Report 92-09, UT, Austin, TX, 1992.
[13] O.C. Zienkiewicz, D.W. Kelly, J. Gago and I. Babuska, in: J. Whiteman, ed., The Mathematics of Finite Elements and Applications IV (1982) 311–346.
[14] O.C. Zienkiewicz and J.Z. Zhu, Comput. Methods Appl. Mech. Engrg. 101 (1992) 207–224.
[15] J.T. Oden, Comput. Methods Appl. Mech. Engrg. 112 (1994) 309–331.
[16] T.J.R. Hughes, Comput. Methods Appl. Mech. Engrg. 127 (1995) 387–401.
[17] W.F. Donoghue, Monotone Matrix Functions and Analytic Continuation (Springer-Verlag, Berlin, 1974).
[18] J.T. Oden and J.N. Reddy, An Introduction to the Mathematical Theory of Finite Elements (Wiley-Interscience, New York, 1976).
[19] O.C. Zienkiewicz and A.W. Craig, in: D.F. Griffiths, ed., The Mathematical Basis of Finite Element Methods, Clarendon Press, Oxford, 1984).
[20] A.J. Baker, Finite Element Computational Fluid Dynamics (Taylor and Francis, Washington, DC).
[21] S.K. Lele, J. Comput. Phys. 103 (1992) 16–42.
[22] D. J. Chaffin and A. J. Baker, Int. J. Numer. Methods Fluids 21 (1995) 273–294.
[23] P. Lax and B. Wendroff, Comm. Pure Appl. Math. 8 (1960) 217–237.
[24] J. Donea, Int. J. Numer. Methods Engrg. 20 (1984) 101–119.
[25] H.L. Stone and P.L.T. Brian, A.I.Ch.E. J. 9 (1964) 681–688.
[26] J. Iannelli, AIAA 96-0763, 34th Aerospace Sciences Meeting, 1996.
[27] S. Roy and A.J. Baker, Int. J. Numer. Heat Trans. 31 (1997) 135–176.
[28] S. Roy, On improved methods for monotone CFD solution accuracy, Ph.D. Thesis, (The University of Tennessee, 1994).
[29] M.S. Liou and B. van Leer, Tech. AIAA 88-0624, 26th Aerospace Meeting, 1988.
[30] Frank M. White, Fluid Mechanics (McGraw Hill, New York, 1979).
[31] S. Roy and A.J. Baker, Comput. Methods Appl. Mech. Engrg. 131 (1996) 209–232.